Materials & Design 223 (2022) 111201

Contents lists available at ScienceDirect

Materials & Design

journal homepage: www.elsevier.com/locate/matdes

Ice-templating hydrogels with high concentrations of cellulose nanofibers to produce architected cellular materials for structural applications

L. Orgéas [a,*], S. Gupta [a,b], F. Martoïa [b], P.J.J. Dumont [b]

[a] Univ. Grenoble Alpes, CNRS, Grenoble INP, 3SR Lab, F-38000 Grenoble, France
[b] Univ. Lyon, INSA-Lyon, CNRS, LaMCoS, UMR5259, 69621 Villeurbanne, France

HIGHLIGHTS

- Highly concentrated hydrogels with cellulose nanofibrils or nanocrystals were ice-templated to produce lightweight architected biosourced foams.
- X-Ray nanotomography and SEM images showed that microstructures of foams switch from anisotropy to isotropy while increasing the nanofiber concentration or aspect ratio.
- Compression results showed that the specific mechanical properties of the foams make them as relevant cellular materials for structural applications.

GRAPHICAL ABSTRACT

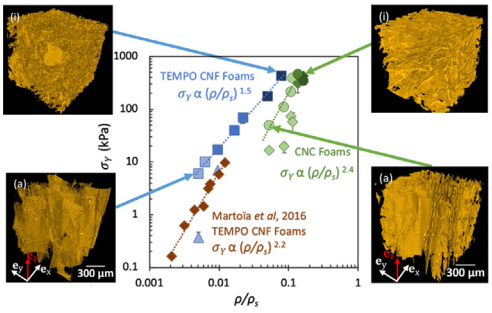

ARTICLE INFO

Article history:
Received 23 June 2022
Revised 17 September 2022
Accepted 22 September 2022
Available online 23 September 2022

Keywords:
Cellulose nanofibril
Cellulose nanocrystal
Structural foam
Ice-templating
Mechanical behaviour
X-ray nanotomography

ABSTRACT

Ice-templated cellular materials made of entangled networks of slender cellulose nanocrystals (CNCs) or cellulose nanofibrils (CNFs) exhibit excellent specific physical properties but their mechanical properties are still insufficient: these biosourced systems cannot be used as structural materials, *e.g.*, as cores of composite sandwich structures. To overcome this limitation, we ice-templated hydrogels with high concentrations of CNFs and CNCs by using a specific setup that enabled their unidirectional solidification. The microstructure and the mechanical properties of the freeze-dried foams were investigated using SEM, X-Ray nanotomography and compression tests, respectively. Increasing the content of nanofibers yielded to drastic shifts of (i) the foam microstructures from highly anisotropic (columnar with CNFs, lamellar with CNCs) to more isotropic ones (ii) the mechanical properties towards isotropy together with a significant increase of the foam stiffness, yield stress and absorbed energy. In addition, due to the high aspect ratio of the CNFs, CNF foams with elevated relative densities exhibit noteworthy specific mechanical properties.

1. Introduction

Crystalline cellulose is one of the major elementary constituents of plant cell walls [1]. It is usually extracted from the vegetal biomass in the form of colloidal aqueous suspensions [2] by using various processing routes [1,2]. Two main categories of cellulose nanomaterials (CNMs) are extracted: (i) cellulose nanofibrils (CNFs) and (ii) cellulose nanocrystals (CNCs). CNCs are generally

* Corresponding author.
E-mail address: laurent.orgeas@3sr-grenoble.fr (L. Orgéas).

https://doi.org/10.1016/j.matdes.2022.111201
0264-1275/

produced via acid hydrolysis of cellulosic fibres suspensions. CNCs exhibit a typical mean length $\bar{l}_{CNC}$ ranging from 100 nm to 200 nm and a typical mean width $\bar{w}_{CNC}$ from 5 nm to 20 nm [3]. Among the various processing routes to produce CNFs, TEMPO–mediated oxidation yields to suspensions of slender nanofibers with electrostatic repulsive forces and a good colloidal stability. CNF suspensions contain slender and mostly crystalline nanofibers with a restrained polydispersity, a typical mean length $\bar{l}_{CNF}$ ranging from 1000 nm to 2000 nm and a typical width $\bar{w}_{CNF}$ from 3 nm to 6 nm, *i.e.*, with aspect ratios $r_{CNF} = \bar{l}_{CNF}/\bar{w}_{CNF}$ at least ten times higher than the CNCs [4–6]. Increasing the concentration of the aforementioned suspensions yields to increase the number of nanofiber-nanofiber contacts so that the suspensions overcome a sol-gel transition to become hydrogels with a solid (gel)-like rheology. CNC or CNF hydrogels can be used to fabricate low-density foams and aerogels with excellent specific physical properties. These cellular materials can be manufactured either via a supercritical processing route [7,8] or via a freeze-drying process, which consists of freezing of the hydrogels followed by the sublimation of the formed ice crystals [9,10]. Freeze-drying appears as a promising processing route to design and tailor architected cellulosic and cellular materials: freeze-dried foams made of TEMPO-oxidised CNFs or CNCs exhibit high porosities, typically ranging from 0.95 to 0.995 and pore sizes of few hundreds micrometres [11–13]. These porous microstructures are practically direct replica of the ice crystals which have nucleated and grown during the freezing phase [14].

The mechanical properties of cellulosic freeze-dried foams, *i.e.*, the elastic moduli in compression (from 1 kPa and 250 kPa) and the yield strengths at the compression plateau (from 50 kPa to 500 kPa) are good [11]. However, they are not sufficient enough to provide the foams the potential to be used for structural lightweight applications in different engineering fields, *e.g.*, as cores of composite sandwich structures in sport, automotive or aeronautic industries. To improve the foam mechanical properties, a better understanding of the following points is required: (i) complex elasto-visco-plastic rheology of cellulose nanofibers hydrogels (which strongly depends on the content but also the aspect ratio of cellulose nanofibers [6,15]), (ii) ice crystal nucleation and growth as functions of the freezing conditions (temperature gradient, solidification rate, mechanical stirring [11,16]), (iii) complex links between the two previous points. Several authors investigated these aspects [9,10,11,13,16]. For example, Martoïa *et al.* [11] explored both the effects of the cooling temperature and the nanofiber content on the microstructures and the mechanical properties of radially ice-templated TEMPO-oxidised CNF foams. The CNF hydrogels used in this study belonged to the concentrated regime (and exhibited elasto-visco-plastic rheology with noticeable yield stress), *i.e.*, with approximately 2 to 8 nanofiber-nanofiber contacts per CNF [6]. The authors reported that the lower the external cooling temperature, the lower the pore sizes of freeze-dried foams, as it has been commonly observed for other ice-templated systems [17]. In addition, anisotropic porous structures with radial columnar pores were observed, similar to the columnar structures observed during the unidirectional freeze-drying of TEMPO-oxidised CNF hydrogels. For comparable CNC concentrations and solidification conditions, Munier *et al.* [18] rather found lamellar pore structures, thus showing an effect of the aspect ratios of nanofibers.

The role of the nanofiber content on the mechanical properties of ice-templated foams was also investigated. For example, Lee and Deng [19] proved that an increase of the CNC content from 0.02 to 0.053 conducted to a non-linear increase of the foam yield strength (or compression plateau stress) from 117 to 290 kPa. Similarly, by increasing the TEMPO-oxidised CNF content from 0.002 to 0.012, Martoïa *et al.* [11] also reported scaling power-laws of the foam Young's moduli and yield strengths with the CNF content, which increased from 3 to 224 kPa and from 0.15 to 10 kPa, respectively. Using 3D *in situ* pore scale observations during compression, the power-law exponents of the scaling laws were correlated with the brittle bending/buckling of the foam cell walls and with the foam consolidation [11].

However, to the best of our knowledge, the effect of the connectivity of the hydrogels on the microstructures and the mechanical properties of ice-templated TEMPO-oxidised CNF or CNC foams was only restrained to the semi-dilute or the concentrated regimes so far. This is probably due to the difficulty to obtain highly concentrated hydrogels, *i.e.*, with more than 5 nanofiber-nanofiber contacts per nanofiber. Thus, exploring these effects with highly concentrated hydrogels is the main objective of this contribution. For that, we processed such hydrogels with TEMPO-oxidised CNFs and CNCs and investigated the evolution of the microstructures of their freezed-dried foams with the nanofiber content and aspect ratio during unidirectional ice-templating. Finally, the improvement of the mechanical properties in compression of the as-processed foams was assessed.

2. Materials and methods

2.1. Native CNF and CNF hydrogels

TEMPO-oxidised CNF hydrogels at a CNF concentration $c_0 = 1.2$ wt.% were supplied by Centre Technique du Papier (Grenoble, France). They were extracted from a bleached kraft wood pulp subjected to a TEMPO-mediated oxidation using a methodology reported by Saito *et al.* [4]. The content of carboxyl groups determined by conductometric titration was 1.5 mmol g^{-1}. CNC powder (spray-dried powder) was supplied by CelluForce (Canada). The content of sulfate half ester groups was 0.25 mmol g^{-1}. The morphological properties of the CNFs and CNCs were studied using scanning (SEM) and transmission (TEM) electron microscopy. The micrographs of Fig. 1a,b prove that the TEMPO-oxidised CNF hydrogels exhibited very few microscale elements, *i.e.*, fragments of fiber cell walls and numerous nanoscale elements, *i.e.*, individualised kinked nanofibers. In addition, Fig. 1c shows that CNC hydrogels contained straight nanofibers. From these micrographs, 100 manual measurements of the width of CNFs and CNC and of the length of CNC were done to estimate their mean values and standard deviations. For the CNF length, only five measurements were carried out due to the difficulty to extract individualised CNF from the micrograph (b), so that only the mean value and its scatter from the min and max values could be obtained in that case. Thus, we got $\bar{w}_{CNF} \approx 7 \pm 2$ nm and $\bar{l}_f \approx 1200 \pm 1200^{+50}_{-300}$ nm and thus a very high aspect ratio $r_{CNF} = \bar{l}_{CNF}/\bar{w}_{CNF} \approx 176$. These data are in line with others reported in the literature [6,20]. Similarly we obtained $\bar{w}_{CNC} \approx 13 \pm 5$ nm and $\bar{l}_{CNC} \approx 160 \pm 74$ nm, thus an aspect ratio r_{CNC} close to 12.5, *i.e.*, more than ten times lower than that of CNFs and in line with literature data [21].

2.2. Preparation of hydrogels

CNF hydrogels were prepared at various concentrations c ranging from 0.45 wt% to 10.6 wt% by diluting or concentrating the native CNF hydrogel at concentration $c_0 = 1.2$ wt.%. For concentrations below c_0, the hydrogel was diluted with deionised water followed by mechanical stirring using a homogenizer (IKA Ultra-Turrax T-18). For concentrations above c_0, the native hydrogel was placed into a vacuum oven heated at 50℃ to progressively dry it until the targeted concentration c was reached. During this

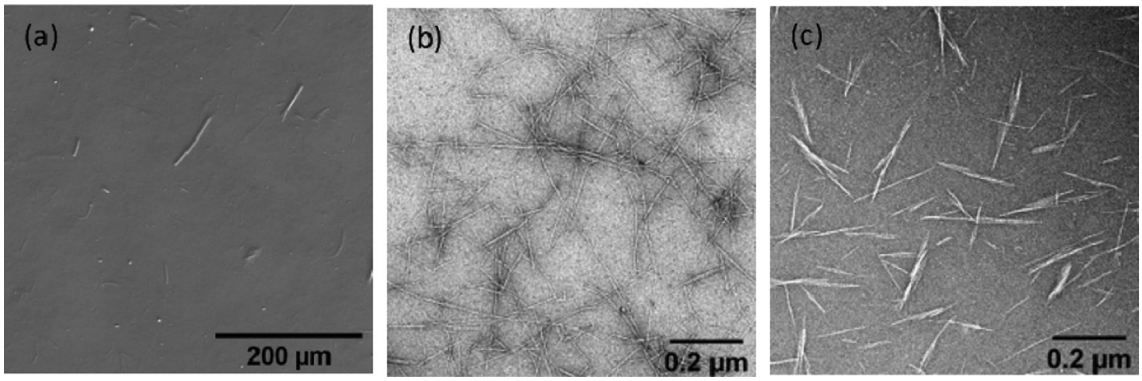

Fig. 1. Micrographs showing (a) remaining partially fibrillated wood fibers in the TEMPO-oxidised CNF hydrogels (SEM), TEMPO-oxidised CNFs (TEM), (c) hydrolysed CNCs.

process, the hydrogel was homogenized every 20 min. Also, CNC hydrogels at concentrations c ranging from 7.7 wt% to 24.6 wt% were prepared by slowly adding the known quantity of CNC powder into deionised water, followed by mechanical stirring (8000–16000 rpm) with the homogenizer until no aggregates were visible. Whatever the type and the concentration of cellulose nanofibers, we measured the pH of the processed hydrogels which systematically ranged between 7 and 7.5, so that these systems could be considered as electrostatically stabilised. The concentration of the CNF or CNC hydrogels was determined using a gravimetric method detailed in [22]. Hence, CNF and CNC hydrogels were processed with nanofiber volume fractions ϕ ranging from 0.003 to 0.073, and from 0.052 to 0.178, respectively. A rough estimate of the corresponding average nanofiber-nanofiber contacts per nanofiber $\bar{z}$ was estimated using the tube model [23] adapted for cellulose nanofibers exhibiting high aspect ratio r and 3D orientation, *i.e.*, $\bar{z} \approx 4\phi r$ [6]. From the lowest to the highest volume fraction of nanofibers, $\bar{z}$ was expected to vary from 2.1 to 51.5 and from 2.6 to 9 for CNF and CNC hydrogels, respectively. Thus, it was possible to progressively switch from concentrated to highly concentrated CNF or CNC hydrogels.

2.3. Fabrication of foams

CNF and CNC foams were fabricated into square plates using unidirectional freezing followed by drying. First, the hydrogel was put inside a mould (Fig. 2b) with a square in-plane surface of lateral dimensions of 40 mm and a height of 10 mm. The mould was composed of two major parts: the container and the lid. The container consisted of a hollow square plate fastened to a basis of a height of 10 mm. As shown in Fig. 2b, the walls of the container were coated with PU foam strips (i) to accommodate the volume expansion induced by the solidification of water during freezing (9% for water) and (ii) to ensure 1D (through the thickness) ice crystal growth during freezing. The lid consisted of a square plate of height 16 mm and of width 80 mm and a piston with a thickness of 2 mm and a width of 50 mm. To freeze the hydrogels, the mould was firstly wrapped inside a thin polyethylene bag (film thickness of 40 µm) and the basis of the mould was placed in contact with a cold silicone oil bath ($-30 \pm 0.2^{\circ}$C, Fig. 2b) of a thermo-regulator (Julabo FP50-HL), so that the freezing of the hydrogels mainly occurred along the mould thickness ($\mathbf{e}_z$-direction). To assess the freezing conditions of the hydrogel, the temperature was recorded using two thermocouples (type K). The thermocouple T_1 was placed in the hydrogel in contact with the mould basis, whereas the thermocouple T_2 was placed in the hydrogel in contact with the lid. Typical time evolutions of T_1 and T_2 are shown in the graph of Fig. 2c. When plunged into the silicone oil bath, the temperature of the hydrogel rapidly fell and started to solidify in the vicinity of the basis at a temperature close to 0 °C at $t \approx 600$ s, where an exothermic peak B-C clearly emphasized the solidification of water at that location. Similarly, the exothermic peak B'-C' at $t \approx 1800$ s also revealed the solidification of water at the top of the sample. Hence, regardless of the investigated cellulose content and type, the ice-templating process typically lasted 1200 s, with a practically constant mean through-thickness temperature gradient of ≈ 1℃ mm^{-1}. The solidification procedure was carried out up to points D and D' ($t \approx 2400$ s). Then, to induce the sublimation of ice crystals, the mould was put inside a freeze dryer (Christ Martin, Alpha 2–4 LD plus) for 48°h at vacuum pressure and temperature set to 0.001 mbar and $-81^{\circ}C$, respectively.

2.4. Structural characterisation

The relative density ρ/ρ_s (or the volume fraction of nanofibers) of each processed foam was estimated by measuring the weight of the foams and their volume to obtain the foam density ρ and by considering the density $\rho_s = 1500\,kg\,m^{-3}$ for cellulose [24,25]. To assess possible shrinkage during freeze-drying, the protocol proposed by Sehaqui *et al.* [26] was adapted to determine the theoretical relative density ρ_t/ρ_s (ρ_t being the theoretical foam density) from the hydrogel concentration c by considering that the pore volume of the foam was equal to the volume of water in the hydrogel plus a 8.6% increase due to the expansion of water during the solidification [17,27]:

$$\rho_t/\rho_s = \frac{c}{\frac{\rho_s}{\rho_w}(1-c)(1+0.086)+c} \tag{1}$$

where $\rho_w \approx 998\,kg\,m^{-3}$ is the water density at room temperature (25℃).

The microstructures of CNF and CNC foams were also analysed using SEM with a HITACHI S-3500 N SEM at 15 kV accelerating voltage in low vacuum pressure (20 Pa). For that, small cubes of foam samples were carefully cut from the parent samples using razor blades, both in parallel and perpendicularly to the freezing direction $\mathbf{e}_z$. Several SEM images were acquired in the $(\mathbf{e}_x, \mathbf{e}_y)$ plane, *i.e.*, perpendicular to the freezing direction. Overlapping images were also recorded along the freezing direction $\mathbf{e}_z$ from the bottom region to the top region of the sample. These overlapping individual images were concatenated using the plugin MosaicJ [28] of the software ImageJ [29].

In addition, the 3D foam microstructures were characterised using an X-ray nanotomograph (RX solutions, France). For that purpose, small foam cubes (2^3 mm^3) were carefully extracted with razor blades from the central region of the parent samples. To investigate the possible heterogeneity of foam samples, two addi-

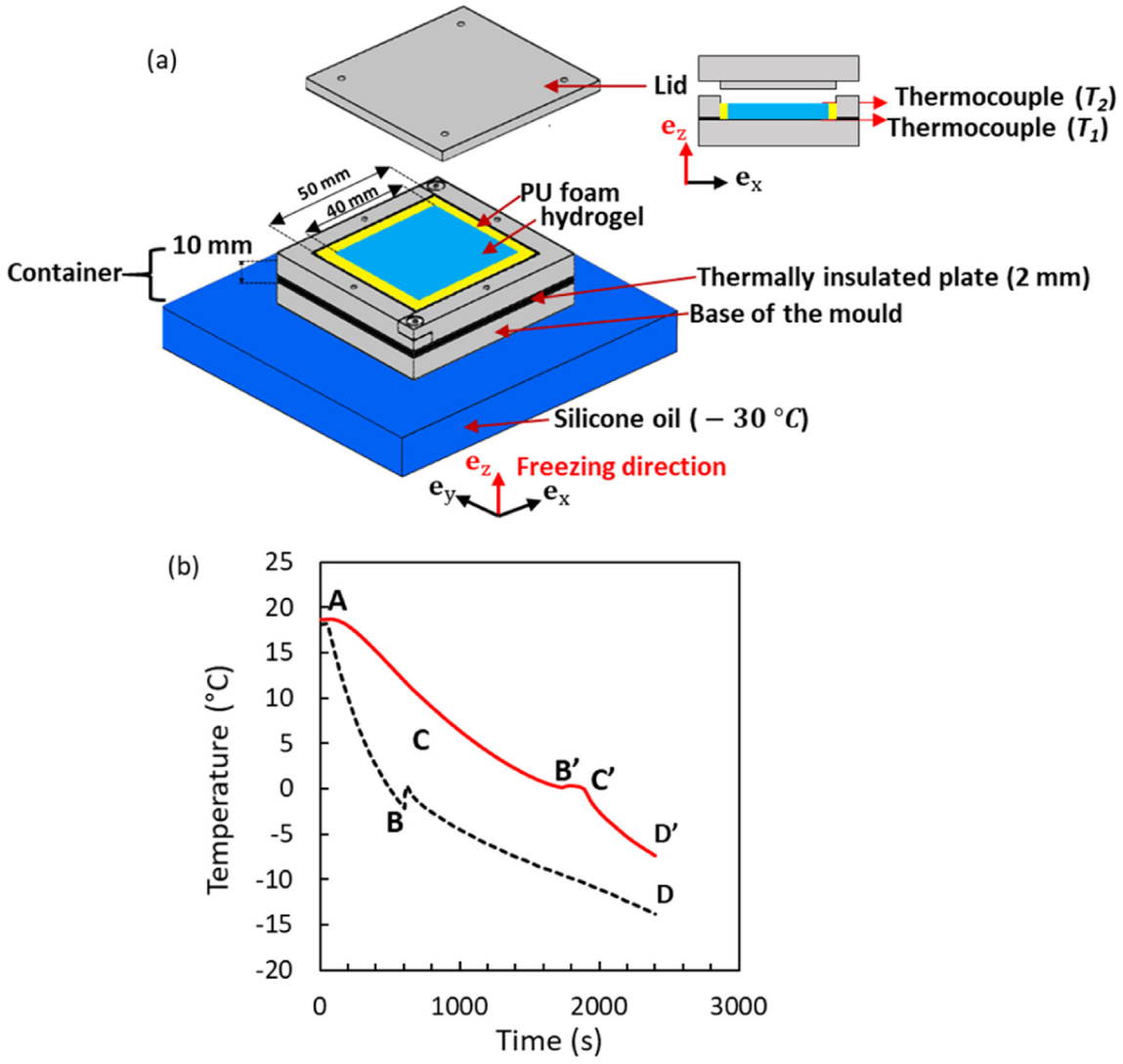

Fig. 2. Sketch of the freezing setup used for the solidification of the CNF and CNC hydrogels (a) and time-evolutions of the temperatures measured in the hydrogel close to the mould lid (continuous line) and basis (dashed line) during the freezing stage (b).

tional cubes were scanned for a CNC foam at $\rho/\rho_s \approx 0.12$ from both the bottom and top regions of the parent sample. During scanning, the X-ray beam energy was set to 60 keV, the voxel size was $1.3^3\ \mu m^3$ and 1233 radiographs were acquired. The 3D images were reconstructed using a filtered back-projection algorithm implemented in software Xact. The region of interest considered for the analysis of the data is $1000^3\ \mu m^3$ from the acquired images to exclude edge effects due to the reconstruction procedure. The 3D images were segmented using the Trainable Weka Segmentation plugin [30] of ImageJ, to enhance the quality of segmentation, in particular for low relative density foams for which the contrast between the pores and the cell wall was rather poor. Thus, 2D slices were first selected from the stack of 3D images acquired for each sample. These slices were used as input data for the training classifier of Weka to obtain nicely segmented images. Then, the degree of anisotropy of the segmented images *DA*, with values close to 0 for isotropic structures and 1 for highly anisotropic ones, was calculated using the mean intercept length (MIL) method implemented in the BoneJ plugin [31]. In addition, the foam mean pore diameter $\bar{d}$ and cell wall thickness $\bar{t}$ were determined using the granulometry function (with octahedron structural elements) of the plugin Analysis 3D [32]. Note that for anisotropic pores, the mean pore diameter $\bar{d}$ corresponds to the smallest pore thickness.

2.5. Mechanical characterization

Uniaxial compression experiments were performed on samples which were carefully cut (with a special procedure that used razor blades) from the Zone 2 of the processed plates (see subsection 3.1), with a height $h_0 = 6\,mm$ along the freezing direction $\mathbf{e}_z$ and square in-plane dimension of size $l_0 = 9\,mm$ (Fig. 3). Most of the compression experiments were performed along the freezing direction $\mathbf{e}_z$. Several compression tests were also performed in a direction perpendicular to the freezing direction to assess the mechanical anisotropy of foams. Before the experiments, the samples were placed under controlled conditions temperature and relative humidity conditions, *i.e.*, $T = 25$℃ and 50% RH (Memmert humidity chamber HCP 150) for 24 h. The experiments were also performed in the same controlled environmental conditions. For that purpose, we used a specially designed chamber connected with a humidity generator (TECHPAP, France), as illustrated in Fig. 3. The chamber surrounded both the compression platens

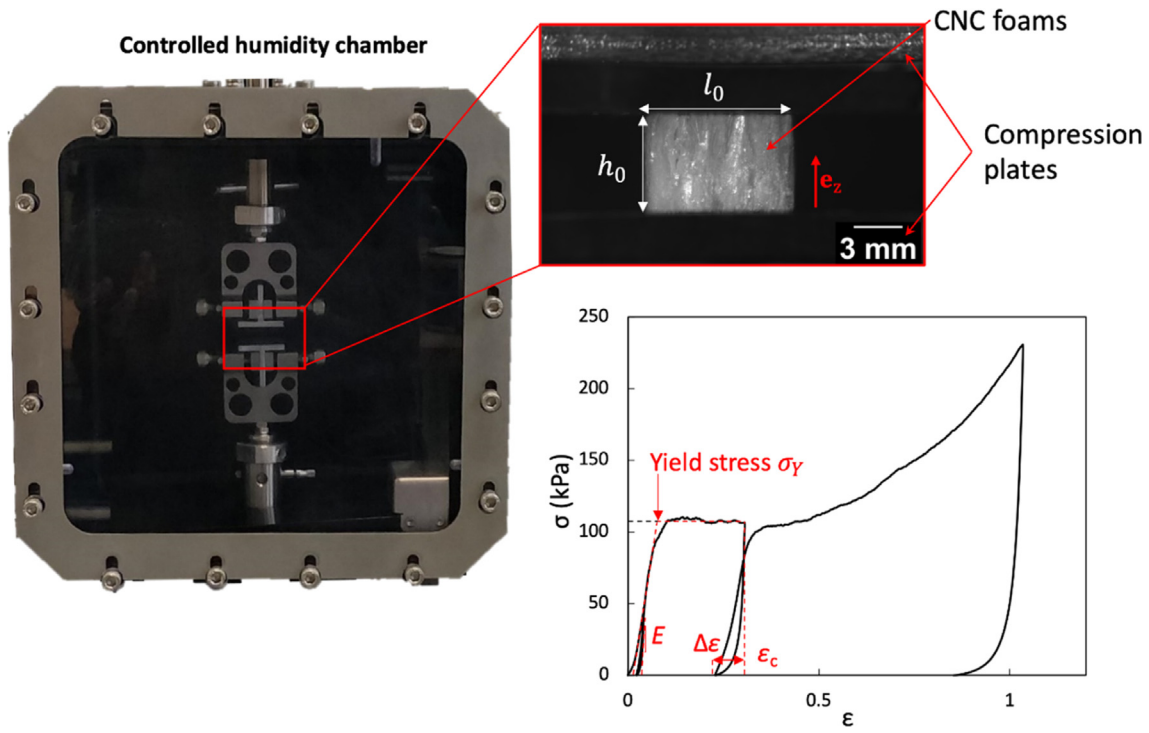

Fig. 3. Compression experimental setup installed in the controlled humidity chamber and mounted on the electromechanical tension–compression machine. The zoom shows a CNC foam sample ($\rho/\rho_s \approx 0.086$) placed between the compression platens before compression along the freezing direction $\mathbf{e}_z$. Below is plotted the corresponding stress–strain curve.

and the sample. The chamber was installed on an electromechanical tension–compression testing machine (INSTRON 5944).

During the tests, the compression force $|F|$ as well as the sample height h and width l (resp. l and h, depending on the sample orientation) were recorded with the load cell, the crosshead displacement and using a digital video camera. The compression strain $\varepsilon = |\ln(h/h_0)|$ and the lateral strain $\varepsilon_l = |\ln(l/l_0)|$ (resp. $\varepsilon = |\ln(l/l_0)|$ and $\varepsilon_l = |\ln(h/h_0)|$) as well as the nominal compression stress $\sigma = |F|/l_0^2$ (resp. $\sigma = |F|/l_0 h_0$) were then estimated. Depending on the strength of samples, three load cells with respective maximal capacities of 10, 100 and 500 N were used. Samples were subjected to three successive load-unload cycles with an initial strain-rate $\dot{\varepsilon}_0 = |v|/h_0$ (resp. $\dot{\varepsilon}_0 = |v|/l_0$) of $0.002\,s^{-1}$, v being the constant crosshead velocity. The first load-unload cycle was carried out in the apparent elastic regime, *i.e.*, with a maximal compression strain $\varepsilon \approx 0.02 - 0.09$. The Young moduli of the foams E was measured during the early stage of the unloading, as schematised in Fig. 3 [33]. The Poisson ratio was also measured in this domain for samples compressed along the freezing direction $\nu = -\varepsilon_l/\varepsilon$. Just above the apparent elastic regime, we estimated the apparent foam yield stress σ_y, as shown in Fig. 3 [11]. To study the foam mechanics at high compression strains, the last unloading was carried out after a compression up to a maximal strain close to 1 from which we estimated the energy (per unit of initial volume) absorbed by the foams during this loading: $W = \int_0^1 \sigma \mathrm{d}\varepsilon$. Likewise, as sketched in Fig. 3, the ratios of the recovery strains $\Delta\varepsilon$ (recorded after unloading) over the strains ε_c attained prior to the second and third unloadings were also determined. For each tested condition, five samples were deformed. Reported data represent the mean values and the error bars were built from the min and max values. In general, the scattering of experimental results was rational for the considered systems, *i.e.*, approx. ±25% around the mean values. The scattering mainly came from (i) the difficulty to cut samples without damaging them (even if a special route was developed to minimise these artefacts) (ii) some rare defects such as isolated big pores induced during solidification. Such a scattering did not alter the trends that will be discussed in the following.

3. Results & discussion

3.1. Microstructures

Relative Density – Fig. 4 shows the evolution of the measured relative densities ρ/ρ_s of the foams with the concentration c of their native hydrogels. The relative densities varied from 0.003 to

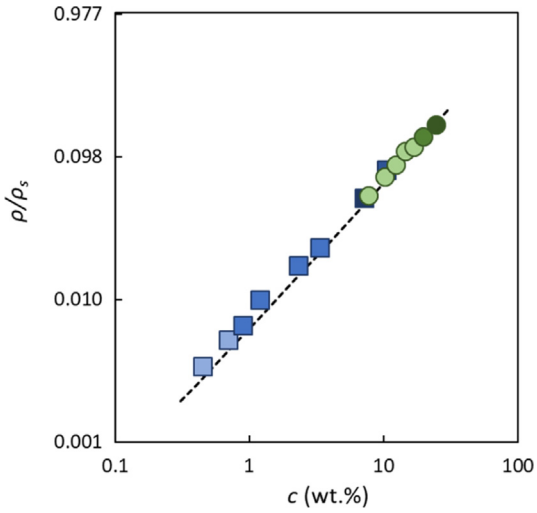

Fig. 4. Evolution of the measured relative density ρ/ρ_s of CNF (square symbols) and CNC foams (circular symbols) with the hydrogel concentration c. The dashed line is the theoretical value ρ_t/ρ_s given by Eq. (1). The differences in the shades represent the transition in the pore microstructures from columnar/lamellar pores (light colours) to more isotropic pores (darker colours).

0.078 for CNF foams and from 0.052 to 0.163 for CNC ones. Please note that foams with high relative densities are not often studied, or even have never been investigated for the highest values [9,10,11,16,26]. In addition, the evolution of the measured relative densities practically followed the theoretical values ρ_t/ρ_s predicted by Eq. (1). Combining this trend with the optical qualitative observations of the foam samples, it is concluded that the freeze-drying route induced limited shrinkage of samples.

Overall microstructures of samples - The SEM micrographs in Fig. 5 show two typical sections of a CNF and a CNC foam along the freezing direction. Regardless of the nanofiber type and content, three distinct zones are revealed and closely linked with the freezing mechanisms emphasised in Fig. 2c. Zone 1 of height close to 0.7 mm corresponds to the colder part of the mould. When water solidification occurred in this zone (points B-C in Fig. 2c), many ice crystals germinated and their growth was restrained due to the supercooling effect of the first stages of freezing [34]. The formation of Zone 1 is difficult to avoid and was observed in other ice-templated systems [16,34,35]. Some authors used a wedge technique [36] to restrain the size of this zone during the ice-templating of hydroxyapatite slurries. This approach could be tested for hydrogels with cellulose nanofibers.

At the top of ice-templated samples another region named Zone 3 with a height close to 1 mm, is also systematically observed. This zone corresponds to another solidification front that was initiated from the top of the mould (points B'-C' in Fig. 2c). A marked solidification front is observed between this descending solidifying Zone 3 and the ascending solidifying Zone 2. It is interesting to notice that the microstructures in Zone 2 strongly differs from those observed in Zone 1 and exhibits practically constant microstructure. These two points are quantified thanks to the analysis of 3D images of CNC samples. In Zone 1, the relative density is slightly higher (0.134) than the mean relative density of the samples (0.115) as emphasized in Fig. 5, whereas it is nearly constant all along Zone 2 (only varying from 0.115 to 0.119 from the centre to the top of this zone). In addition, the degree of anisotropy *DA*, the mean pore diameter $\bar{d}$ and wall thickness $\bar{t}$ in Zone 1 are equal to 0.7, 39.3 μm and 7.8 μm, respectively, showing that the resulting foams exhibit small pores with limited anisotropy. On the contrary, in the centre (resp. the top) of Zone 2, these descriptors are practically constant and respectively equal to 0.81 (resp. 0.88), 76 μm (resp. 88 μm), and 16 μm (resp. 15 μm). Clearly, the microstructure in Zone 2 is almost homogeneous and exhibits larger pores with higher anisotropy. Similar conclusions about the foam homogenity in Zone 2 can be drawn for the whole set of investigated foams. Thus, in the following, both the microstructures and the mechanical properties will be investigated on specimens which were carefully extracted from Zones 2 only.

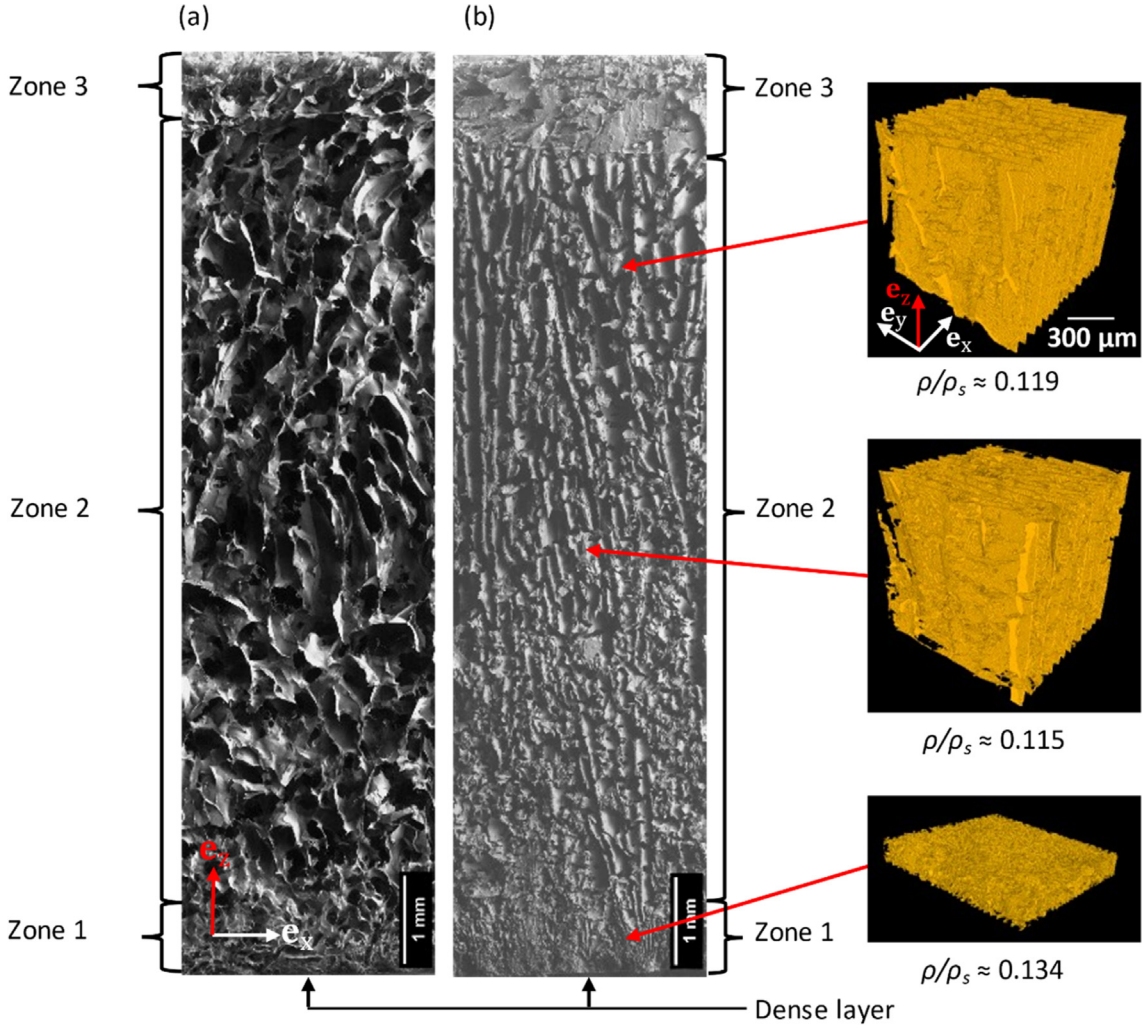

Fig. 5. SEM micrographs of a CNF foam ($\rho/\rho_s = 0.01$)(a) and CNC foam ($\rho/\rho_s = 0.115$)(b), showing sections along the freezing direction $\mathbf{e}_z$ with the three different zones 1, 2 and 3 induced during ice-templating. The red arrows indicate where the 3D images (on the right, X-Ray nanotomography) of CNC foams were acquired.

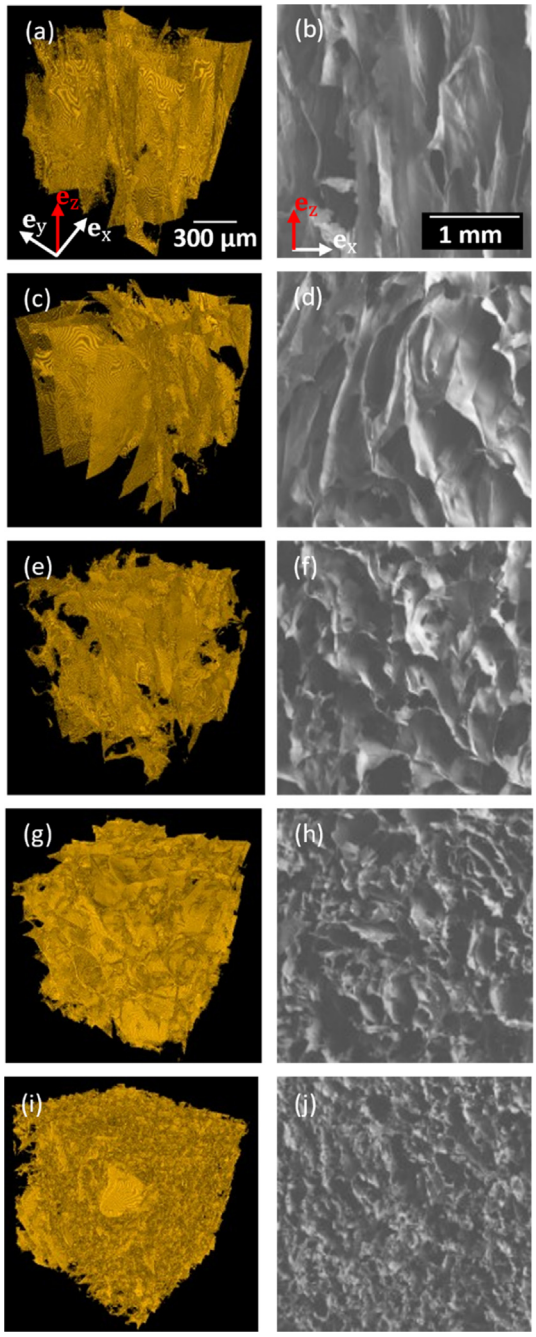

Fig. 6. 3D (X-Ray nanotomography) (left) and 2D (SEM) micrographs (right) showing the structures of CNF foams along the freezing direction $\mathbf{e}_z$ within Zone 2 at various studied relative densities ρ/ρ_s : 0.003 (a, b), 0.0063 (c, d), 0.01 (e, f), 0.05 (g, h) and0.079 (i, j).

Effect of relative density and type of cellulose nanofibers – The collection of micrographs shown in Figs. 6-9 reveals the microstructures of the central zones (Zone 2) of CNF and CNC foams produced at various relative densities ρ/ρ_s. Combined with Fig. 10, which gives the evolutions of the quantitative microstructure descriptors with the relative density and the type of cellulose nanofibers (estimated from the 3D images), these micrographs bring up the following comments:

- For CNF foams, important microstructure variations are observed while increasing the relative density ρ/ρ_s. For example, at standard relative densities ($\rho/\rho_s < 0.0063$), the foams exhibit columnar structures with slender pores which are orientated along the freezing direction $\mathbf{e}_z$ with more or less isotropic shapes in the perpendicular $(\mathbf{e}_x, \mathbf{e}_y)$ plane. This is revealed by scrutinizing the micrographs shown in Fig. 6a-d and Fig. 7a, respectively. These observations are also in line with those already reported for these relative densities, type of TEMPO-oxidised CNFs, and ice-templating processing conditions [16]. Such "columnar" structures exhibit large mean pore sizes $\bar{d}$ around 275 µm (Fig. 10c) and high values of the degree of anisotropy *DA* close to 1 (Fig. 10a). For those concentrations, the rheological properties (yield strength and viscosity) of the CNF hydrogels were presumably sufficiently low enough to allow the growth of ice-crystals towards the temperature gradient direction $\mathbf{e}_z$ [15]. However, a radical alteration of the CNF foam microstructures occurred when processing them with highly concentrated native hydrogels, *i.e.*, for foams with $\rho/\rho_s > 0.01$ (Fig. 6e-f). Indeed, as emphasised in Fig. 6g-j, the pore structures switch from columnar ones to much less anisotropic ones, with more spheroidal pores. This is illustrated in Fig. 10a where a substantial decrease of *DA* is observed in this regime, towards values close to 0.2. In parallel, the anisotropy decrease is accompanied with a noticeable decrease of the mean pore size $\bar{d}$ down to 90 µm (Fig. 10c). These two combined observations prove that the rheological properties of the highly concentrated hydrogels were presumably "hard" enough [15] (i) to restrain ice-crystal growth, in particular along the freezing direction and (ii) to promote ice-crystal nucleation. Lastly, the graph plotted in Fig. 10b shows that the thickness of cell walls significantly increases with ρ/ρ_s (from $\approx 3\mu$m to $\approx 10\mu$m), regardless of the concentration regime of the CNF hydrogels.
- For CNC foams, some of the aforementioned trends are also valid, although noticeable differences explained hereafter are observed. For example, producing CNC foams with relative densities below 0.135, *i.e.*, from CNC hydrogels with "soft" enough rheological properties [15], also yielded to highly anisotropic structures, as illustrated in Fig. 8a-f. Ice-crystal growth along the freezing direction $\mathbf{e}_z$ is privileged with respect to ice-crystal nucleation. The estimated degree of anisotropy *DA* is also similar to those found for CNF foams at much lower relative

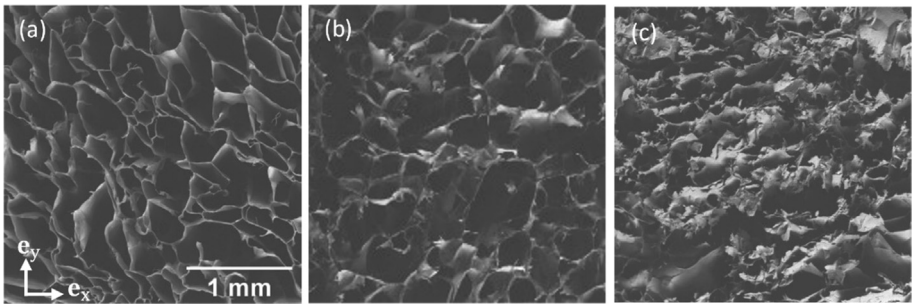

Fig. 7. SEM micrographs showing the structures of CNF foams perpendicular to the freezing direction $\mathbf{e}_z$ within Zone 2 at various relative densities $\rho/\rho_s = 0.003$ (a), 0.01 (b) and 0.05 (c).

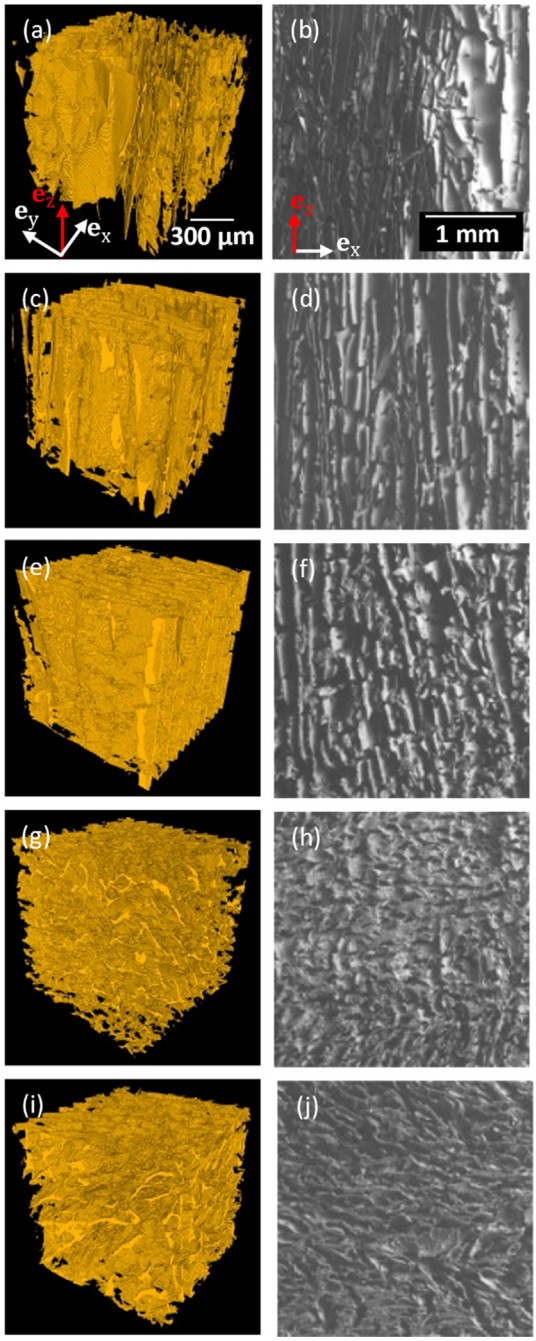

Fig. 8. 3D (X-Ray nanotomography) (left) and 2D (SEM) micrographs (right) showing the structures of CNC foams along the freezing direction $\mathbf{e}_z$ within Zone 2 at various relative densities $\rho/\rho_s = 0.052$ (a, b), 0.086 (c, d), 0.115 (e, f), 0.135 (g, h) and 0.164 (i, j).

densities. This is probably related to the much higher aspect ratio r_{CNF} with respect to r_{CNC} [13]. Indeed, to get similar rheological properties and thus analogous interactions with ice crystals during ice-templating, the concentration of the CNC hydrogels must be much higher than that of the CNF hydrogels. In addition, in this anisotropic growth regime, it is interesting to notice that the mean pore size $\bar{d}$ is much smaller for CNC foams than for CNF ones (Fig. 10c). A close look at the micrographs shown in Fig. 7a and Fig. 9a can explain this result: the columnar ice-crystal growth observed for CNF foams rather looks like to lamellar growth for CNC ones. Hence, the corresponding CNC foam exhibits anisotropic lamellar substructures in the $(\mathbf{e}_x, \mathbf{e}_y)$ planes. The reasons to explain the difference of pore morphology between CNF foams (columnar) and CNC foams (lamellar) remain unclear. Possible explanations could lie again in the differences in the rheological properties of the CNF and CNC hydrogels [15], and more particularly to those related to the aspect ratios and the physico-chemical interactions of the two types of cellulose nanofibers. The aspect ratio hypothesis is probably interesting to further analyse as CNCs exhibit a moderate aspect ratio r_{CNC} and CNC foams lamellar structures similar to those observed for ice-templated suspensions with granular or platelets particles [17]. In addition, a transition from highly lamellar microstructures to less lamellar and more isotropic ones is observed above the relative density of 0.135, whilst ice-templating highly concentrated hydrogels. This is evidenced in Fig. 8g-i and Fig. 9b,c, as well as in Fig. 10. Finally, Fig. 10b also illustrates the important increase of the thickness of the CNC foam cell walls with the relative density (from $\approx 9\mu$m to $\approx 31\mu$m), in accordance with the trend observed with CNF foams.

3.2. Mechanical properties in compression

Typical behaviour – The stress–strain curves displayed in Fig. 11 show the typical mechanical responses of CNF (a,c) and CNC foams (b,d) at standard (a,b) or high (c,d) relative densities. Photographs of samples at various compression strains are shown in this figure to reveal the mesoscale deformation mechanisms at the origin of the macroscale stress–strain response.

- Regardless of the relative densities, sample orientation and type of cellulose nanofibers, stress–strain curves exhibit shapes that are similar to those observed during the compression of elasto-plastic or brittle foams [37] and those obtained for ice-templated foams [11,38]. Three distinct stages are observed. In a first stage at small compression strains, a sharp increase of the stress is measured and often ascribed to the elastic compression and bending of the foam cell walls. In this stage, the Poisson's ratio v of the samples is systematically $\ll -0.5$, thus proving that all tested foams consolidated in this regime too. This result is similar to that reported by Martoïa *et al.* [11] for CNF foams at low relative densities ($\rho/\rho_s < 0.006$) and for which an auxetic effect was also found with Poisson's ratios close to -0.6. However, the auxetic behaviour is lost for higher relative densities: the Poisson's ratio is positive and never exceeded 0.08. For CNC foams, the Poisson's ratio was always positive with values around 0.1–0.15, still emphasizing foam consolidation. This figure also reveals that even in this regime, CNF and CNC foams exhibit elastoplasticity: non zero-valued residual strains are observed. This regime is ended at a yield strength σ_y above which a second consolidation regime occurs. The second regime is usually ascribed to the elastoplastic deformation or damage of cell walls [37]. Herein, stress levels increase or slightly decrease, depending on the involved predominant microstructure deformation mechanisms. Finally, when the relative density is sufficiently high, the consolidation become more difficult: a third regime with a sharp increase of stress levels is observed.
- In general, for the studied foams, the second consolidation regime occurred with a slight (CNC) or pronounced (CNF) hardening of stress levels, except for CNC foams deformed along the freezing direction $\mathbf{e}_z$ for which an horizontal stress plateau (Fig. 11d) or even a softening of stress levels was observed (Fig. 11b). For CNF foams, the consolidation is rather homogeneous (*cf.* photographs in Fig. 11a,c) and could be correlated

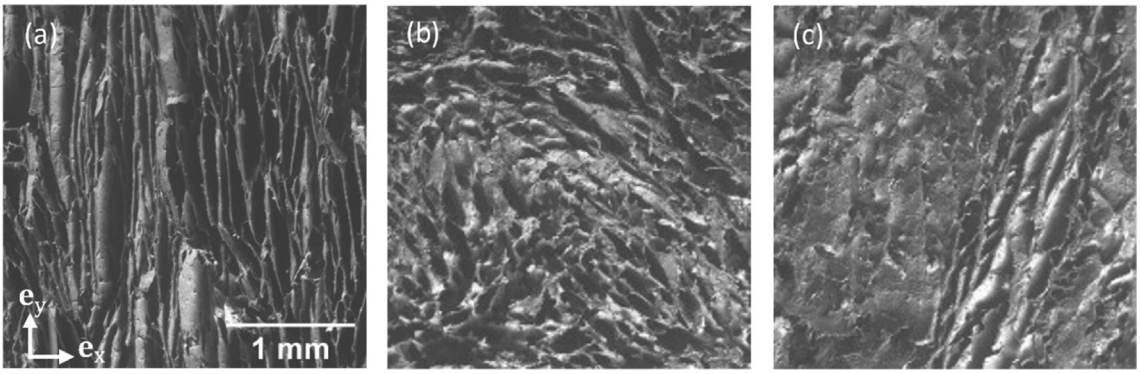

Fig. 9. SEM micrographs showing the microstructures of CNC foams perpendicular to the freezing direction $\mathbf{e}_z$ in Zone 2 at various relative densities $\rho/\rho_s = 0.108$ (a), 0.135 (b) and 0.164 (c).

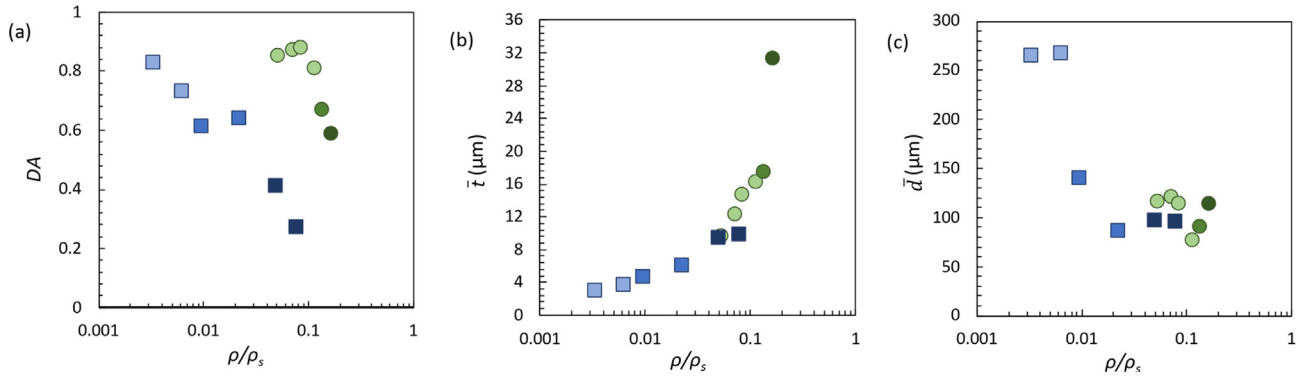

Fig. 10. Evolutions with the relative density ρ/ρ_s of the degree of anisotropy *DA* (a), the mean cell wall thickness $\bar{t}$ (b) and the mean pore thickness $\bar{d}$ for TEMPO-oxidised CNF foams (square symbols) and CNC foams (circular symbols). The differences in the shades represent the transitions in the pore microstructures, from columnar/lamellar pores (light colours) to more isotropic pores (darker colours).

to the stress hardening. On the contrary, heterogeneous damage bands or large damaged zones systematically appeared in CNC foams. Small shear bands were observed between the lamellar domains in the $(\mathbf{e}_x, \mathbf{e}_y)$ plane during the compression of CNC foams perpendicular to the freezing direction, whereas large damage zones were observed during the compression tests along the freezing direction (Fig. 11b). These brittle deformation *meso*-mechanisms could be correlated to the small hardening or softening of stress levels, respectively.

- At standard relative densities, where highly anisotropic microstructures are observed (see last subsection), stress–strain curves also depend on the loading direction, regardless of the investigated type and content of cellulose nanofibers. This is illustrated in Fig. 11a,b and in-line with the literature data [13]. Compression along the freezing direction, *i.e.*, along the main orientation of pores and pore cell walls, yielded to a stiffer mechanical behaviour and higher stress levels, but in turn to lower strain recovery $\Delta\varepsilon$ after unloading.
- The effect of the nanofiber content (or the foam relative density ρ/ρ_s) and aspect ratio is also evidenced. On the one hand, increasing the nanofiber content of the hydrogels from the concentrated regime (Fig. 11a,b) to the highly concentrated regime (Fig. 11c,d) leads a significant increase in their stiffness and stress levels. On the other hand, the comparison of Fig. 11a and Fig. 11b and the comparison of Fig. 11c and Fig. 11d shows that increasing the aspect ratio of the nanofibers (case of CNFs *vs.* CNCs) at constant nanofiber content enables obtaining foams exhibiting higher stress levels. These two points will be further discussed hereafter.

Effect of the relative density and aspect ratio of cellulose nanofibers – The two first graphs of Fig. 12 show the evolution of the Young's modulus E and yield strength σ_y of the foams with ρ/ρ_s. For comparison, we also added the data obtained by Martoïa *et al.* [11] for similar TEMPO oxidised CNFs and relative densities. Only the foams which microstructures were close to ours were used, *i.e.*, the ones which were processed with radially orientated solidification temperature gradients, with monomodal elongated pore cell walls mainly orientated perpendicular to the freezing direction $\mathbf{e}_z$ of the current study. The two last graphs also give the evolutions of the absorbed energy and the recovery ratio $\Delta\varepsilon/\varepsilon_c$ (along the freezing direction) with the relative densities for the two types of foams. Several remarks can be drawn from this figure:

- As all other foams [37], the Young's modulus E and the yield strength σ_y of CNF and CNC foams follow scaling laws in the form of power-law functions of the relative density ρ/ρ_s, *i.e.*, $E \propto (\rho/\rho_s)^n$ and $\sigma_y \propto (\rho/\rho_s)^m$. The scaling exponents $n = 1.7$ and $m = 1.5$ obtained for CNF foams (along the freezing direction $\mathbf{e}_z$) are consistent with those reported in earlier studies [11,26]. Also, they are close to those expected for classical cellular materials with regular microstructures such as open ($n = 2$ and $m = 1.5$) or closed foams without thickening of edges ($n = 3$ and $m = 2$) [33,37]. These exponents are consistent with deformation micro-mechanisms governed by plate and strut bending of idealised cell walls. This scenario has already been checked by 3D *in situ* cell wall scale observations carried out by Martoïa *et al.* [11] where the TEMPO CNF foam deformation was induced by the bending/buckling of both ridges and thin

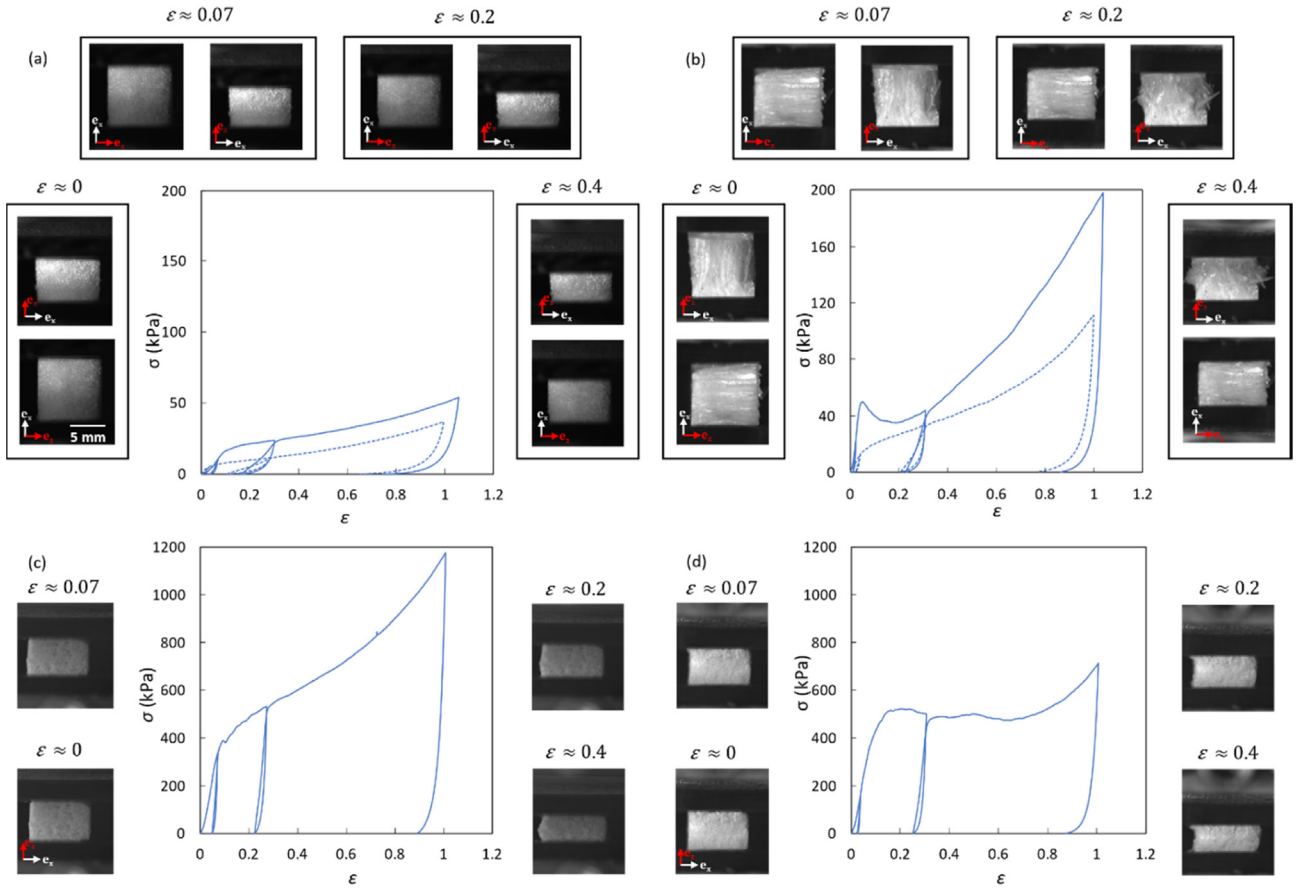

Fig. 11. Typical stress–strain curves for CNF (a, with $\rho/\rho_s \approx 0.01$ and c, with $\rho/\rho_s \approx 0.078$) and CNC foams (b, with $\rho/\rho_s \approx 0.052$ and d, with $\rho/\rho_s \approx 0.135$). The photographs show deformed samples at various strains. At standard relative densities (a,b), as the foams exhibited anisotropic properties, the graphs show the compression responses along the freezing direction $\mathbf{e}_z$ (solid line) and perpendicular to it (dashed line) with corresponding photographs of the samples at various strains.

walls of cells. The exponents obtained for CNC foams are also similar, albeit slightly higher, suggesting similar deformation mechanisms at the cell wall scale. In addition, they are close to those estimated in previous studies for other ice-templated systems with lamellar microstructures [17,39].

- As shown in Fig. 12a,b, results obtained for standard relative densities and perpendicular to the freezing direction are quantitatively consistent with those obtained by Martoïa *et al.* [11] for radially ice-templated CNF foams with monomodal elongated pores that were also perpendicular to the compression direction. This shows the relevance of the current data and tends to prove that similar cell wall deformation mechanisms occur for these two types of ice-templated TEMPO-oxidised CNF foams. In addition, still for these standard relative densities, both the foam stiffness and stress levels are much higher when measured along the freezing direction. This result shows a similar behaviour than that of regular honeycomb structures [37] and can be explained by the orientation of cell walls which are preferentially aligned along the compression axis.
- Furthermore, as emphasized in Fig. 12a,b for CNF foams, switching from standard relative densities to high relative densities, *i.e.*, only by multiplying the CNF content of native hydrogels by a factor 10 (from 0.007 to 0.07), yields to multiply the Young's modulus E and the yield strength σ_y by factors of approximately 100 and 40, respectively. This outstanding reinforcement makes these systems as potentially interesting lightweight structural materials, *e.g.*, for cores of sandwich structures for sport, automotive, aeronautics and packaging industries. It is accompanied by a decrease of the mechanical anisotropy, in accordance with the foam microstructural evolution shown in Fig. 10a. The highest CNF content would lead to the most performant structural foam, with the highest specific stiffness E/ρ and specific strength σ_y/ρ [40]. CNC foams with high relative densities are also attractive, but less than CNF foams, as higher CNC content is required to reach equivalent mechanical properties. This is probably ascribed to the lower aspect ratio of CNC nanofibers [6].
- Fig. 12c shows that for a maximal compression strain ε_{max} of 1, the energy absorbed by the foam W during loading increased in power-law with the relative density, regardless of the considered type of nanofibers. For CNF foams, the power-law exponent is close to 1.6, whereas it reaches 2 for CNC foams. Interestingly, at fixed relative density, the absorbed energy is always at least five times higher for CNF foams than for CNC ones. Hence, if for a given application (*e.g.*, packaging) a given value of absorbed energy is required together with the lowest mass for the absorbing component, CNF foams should be preferred.
- Fig. 12d proves that for standard relative densities (lighter symbols) the recovery ratio $\Delta\varepsilon/\varepsilon_c$ decreases with the increase in the compression strain ε_c, regardless of the nanofiber type. The recovery ratio $\Delta\varepsilon/\varepsilon_c$ is high but largely below 1 in the apparent elastic regime, thus proving again that even in this regime, a probable foam damage-induced plasticity occurred. It is worth mentioning that the ratio $\Delta\varepsilon/\varepsilon_c$ is higher for CNF foams where the non-linear elastic recovery is the most efficient for these standard relative densities. For example, for practically identical stress levels (Fig. 11a and Fig. 11b) the recovery ratio is close to

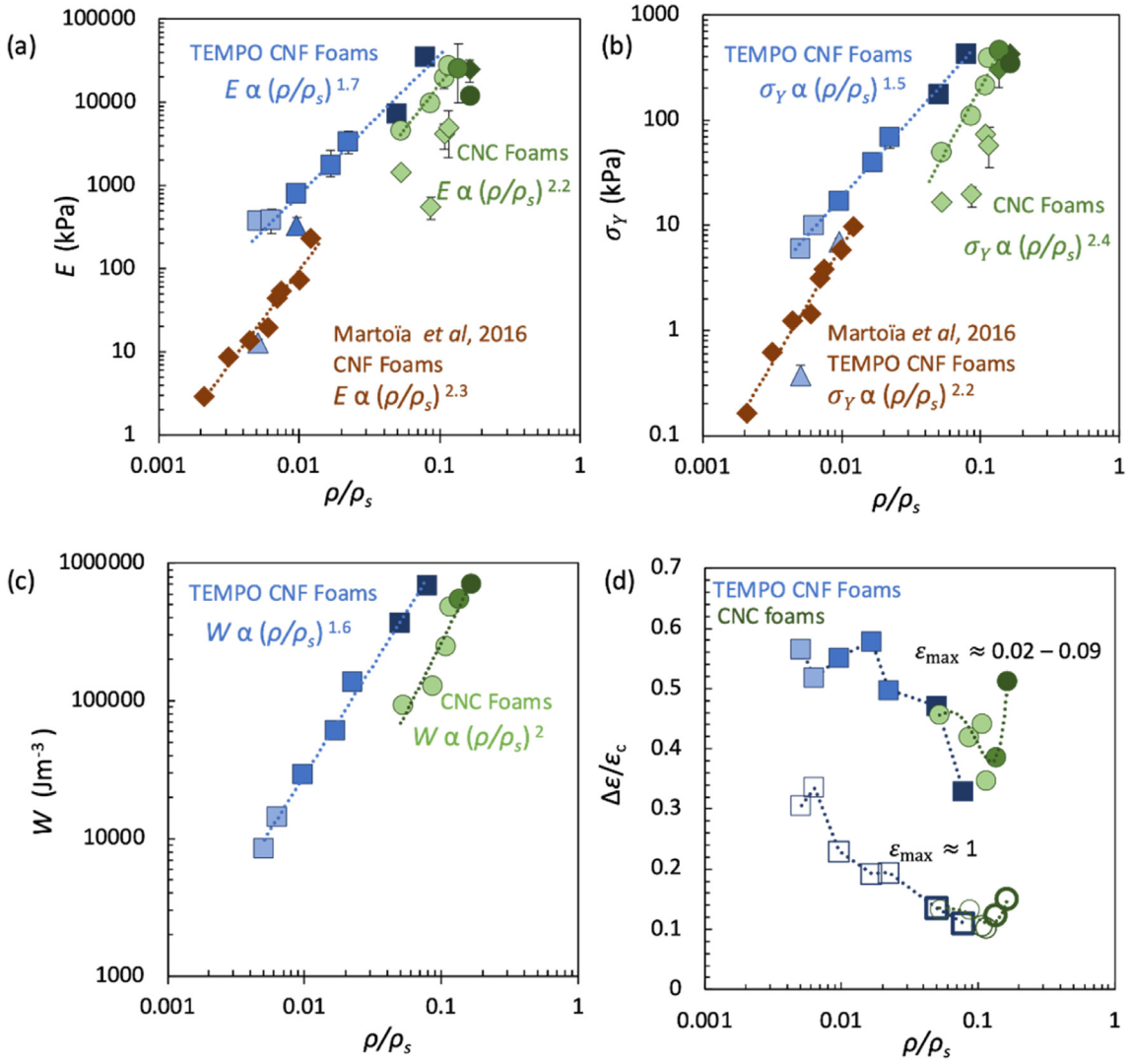

Fig. 12. Evolutions with the relative density ρ/ρ_s of the CNC (green circular symbols) or CNF (blue square symbols) Young's moduli E (a), yield stress σ_y (b), absorbed energy per unit volume W (c) and strain recovery ratio $\Delta\varepsilon/\varepsilon_c$ (d). Squares or circles and triangles or diamonds are the data obtained in directions parallel and perpendicular to the freezing direction, respectively. Graphs (a) and (b) also show the data obtained by Martoïa *et al.* [11] for TEMPO-oxidised foams with radial (anisotropic) ice-templating. The difference in the shades represents the transitions in the pore microstructures, from columnar/lamellar pores (light colours) to more isotropic pores (darker colours).

0.22 after a compression strain of 1 for CNF foams, whereas it only reaches 0.14 for CNC foams. It is interesting to notice that this trend is reversed as high relative density foams are considered (darker symbols in Fig. 12). Still with practically identical stress levels, Fig. 11c and Fig. 11d show that the recovery ratio is close to 0.1 after a compression strain of 1 for CNF foams, whereas it is still close to 0.14 for CNC foams. Astonishingly, for CNC foams, Fig. 12d shows that the recovery ratio is even improved as the relative density is increased.

4. Conclusion

We investigated the microstructures and the mechanical properties of ice-templated TEMPO-oxidised CNF and CNC foams. A focus was made on foams processed from hydrogels with high concentrations of cellulose nanofibers to investigate the capabilities of the resulting foams to be used as structural architected cellular materials. For that, (highly) concentrated hydrogels were ice-templated with unidirectional solidification and characterized, with the following main outcomes:

- Regardless of the concentration and the type of nanofibers in the hydrogels, micrographs showed that the solidification yielded to important microstructure gradients along the solidification direction with two upper and lower zones of small heights, and a large bulk zone. In the latter zone, the foam microstructures display homogeneous microstructure with nearly constant structural descriptors.
- In the bulk zone, foams obtained from hydrogels with standard concentrations exhibit slender pores aligned along the freezing direction. These pores have lamellar shapes for CNCs, as reported earlier for such moderately slender nanoparticles or for other systems made of granular ceramics nanoparticles. The pore microstructures of CNF foams are very different with pores of columnar shapes. This is probably related to the high slenderness of CNFs and their entanglements in the hydrogels.
- For both type of hydrogels, increasing the nanofiber concentration yields to switch from anisotropic to more isotropic porous structures with finer pore size and thicker cell walls. This transition emphasises the key role of the rheology of the hydrogels [15] that could probably restrain ice crystal growth and enhances ice crystal nucleation with the increase in the nanofi-

ber content and/or aspect ratio. Due to the higher aspect ratio of CNFs, this transition occurs at higher concentrations for CNC hydrogels than for CNF hydrogels [15]. Increasing the temperature gradient during ice-templating would probably result in shifting this structural transition.

- Regardless of the concentration and type of nanofibers, the mechanical behaviour of ice-templated foams is elasto-plastic with marked consolidation, even in the apparent elastic regime. The origin of this plasticity is probably cell wall damage induced by their bending/buckling [11]. The damages occur more homogeneously and the consolidation is more pronounced for CNF foams so that the foams exhibit stress hardening during compression. On the contrary, large damage zones appeared in CNC foams, which sometimes result in strain softening during compression. In any case, these damages conduct to limited strain recovery ratio after unloading. For that purpose, supporting the strength of physical bonds between the nanofibers of the foam cell walls (hydrogen, electrostatic, van der Waals bonds), *e.g.,* by adding covalent cross-links with functionalised nanofibers [41] or by adding a polymer matrix to form elasto-plastic or hyperelastic nanocomposite cell walls [42] would undoubtedly be relevant solutions to enhance the mechanics of these foams.
- For standard relative densities, results are consistent with those obtained earlier with the same type of CNF foams. They emphasise the marked mechanical anisotropy of the foams, which is directly related to the high degree of structural anisotropy of the foams that was quantified from 3D micrographs for the first time. Increasing the nanofiber content and aspect ratio leads to substantial improvement of the foam stiffness, yield strength, and absorbed energy in compression. In particular, CNF foams exhibit interesting specific mechanical properties for light-weight structural applications.

Declaration of Competing Interest

The authors declare that they have no known competing financial interests or personal relationships that could have appeared to influence the work reported in this paper.

Acknowledgments

This research was supported by IDEX Université Grenoble Alpes (IRS Project Nanocell²) and Labex Tec21. The authors gratefully acknowledge LabEX Tec 21 and the research site of INSA Lyon at Oyonnax for administrative and technical support. The authors also thank J.-L. Putaux (CERMAV) and S. Rolland du Roscoat for their respective support in the experiments performed using the transmission electron microscope and the X-Ray nanotomograph. The laboratory 3SR is part of the LabEx Tec 21 (Investissements d'Avenir-grant agreement n°ANR-11-LABX-0030) and the Carnot Institute Polynat (n°ANR16-CARN-0025).

References

[1] A. Dufresne, Nanocellulose: From Nature to High Performance Tailored Materials, Walter de Gruyter GmbH & Co KG, 2017.
[2] O. Nechyporchuk, M.N. Belgacem, J. Bras, Production of cellulose nanofibrils: A review of recent advances, Ind. Crops Prod. 93 (2016) 2–25, https://doi.org/10.1016/j.indcrop.2016.02.016.
[3] D. Klemm, E.D. Cranston, D. Fischer, M. Gama, S.A. Kedzior, D. Kralisch, F. Kramer, T. Kondo, T. Lindström, S. Nietzsche, K. Petzold-Welcke, F. Rauchfuß, Nanocellulose as a natural source for groundbreaking applications in materials science: Today's state, Mater. Today 21 (7) (2018) 720–748, https://doi.org/10.1016/j.mattod.2018.02.001.
[4] T. Saito, Y. Nishiyama, J.-L. Putaux, M. Vignon, A. Isogai, Homogeneous Suspensions of Individualized Microfibrils from TEMPO-Catalyzed Oxidation of Native Cellulose, Biomacromolecules 7 (6) (2006) 1687–1691, https://doi.org/10.1021/bm060154s.
[5] F. Martoïa, C. Perge, P.J.J. Dumont, L. Orgéas, M.A. Fardin, S. Manneville, M.N. Belgacem, Heterogeneous flow kinematics of cellulose nanofibril suspensions under shear, Soft Matter 11 (24) (2015) 4742–4755, https://doi.org/10.1039/C5SM00530B.
[6] F. Martoïa, P.J.J. Dumont, L. Orgéas, M.N. Belgacem, J.-L. Putaux, Micro-mechanics of electrostatically stabilized suspensions of cellulose nanofibrils under steady state shear flow, Soft Matter 12 (6) (2016) 1721–1735, https://doi.org/10.1039/C5SM02310F.
[7] K. Sakai, Y. Kobayashi, T. Saito, A. Isogai, Partitioned airs at microscale and nanoscale: thermal diffusivity in ultrahigh porosity solids of nanocellulose, Sci. Rep. 6 (2016) 20434, https://doi.org/10.1038/srep20434.
[8] L. Heath, W. Thielemans, Cellulose nanowhisker aerogels, Green Chem. 12 (2010) 1448–1453, https://doi.org/10.1039/C0GC00035C.
[9] S. Gupta, F. Martoïa, L. Orgéas, P.J.J. Dumont, Ice-templated porous nanocellulose-based materials: current progress and opportunities for materials engineering, Appl. Sci. 8 (2018) 2463, https://doi.org/10.3390/app8122463.
[10] N. Lavoine, L. Bergström, Nanocellulose-based foams and aerogels: processing, properties, and applications, J. Mater. Chem. A 5 (2017) 16105–16117, https://doi.org/10.1039/C7TA02807E.
[11] F. Martoïa, T. Cochereau, P.J.J. Dumont, L. Orgéas, M. Terrien, M.N. Belgacem, Cellulose nanofibril foams: Links between ice-templating conditions, microstructures and mechanical properties, Mater. Des. 104 (2016) 376–391, https://doi.org/10.1016/j.matdes.2016.04.088.
[12] C. Jiménez-Saelices, B. Seantier, B. Cathala, Y. Grohens, Spray freeze-dried nanofibrillated cellulose aerogels with thermal superinsulating properties, Carbohydr. Polym. 157 (2017) 105–113, https://doi.org/10.1016/j.carbpol.2016.09.068.
[13] Y. Chen, L. Zhou, L. Chen, G. Duan, C. Mei, C. Huang, J. Han, S. Jiang, Anisotropic nanocellulose aerogels with ordered structures fabricated by directional freeze-drying for fast liquid transport, Cellulose 26 (11) (2019) 6653–6667, https://doi.org/10.1007/s10570-019-02557-z.
[14] S. Deville, Ice-templating, freeze casting: Beyond materials processing, J. Mater. Res. 28 (2013) 2202–2219, https://doi.org/10.1557/jmr.2013.105.
[15] P.J.J. Dumont, S. Gupta, F. Martoïa, L. Orgéas, Elongational behaviour of electrostatically stabilised and concentrated CNF and CNC hydrogels: experiments and modelling, Carbohydr. Polym (In Revision). (2022).
[16] C. Jiménez-Saelices, B. Seantier, B. Cathala, Y. Grohens, Effect of freeze-drying parameters on the microstructure and thermal insulating properties of nanofibrillated cellulose aerogels, J. Sol-Gel. Sci. Technol. 84 (3) (2017) 475–485, https://doi.org/10.1007/s10971-017-4451-7.
[17] S. Deville, Freezing Colloids: Observations, Principles, Control, and Use: Applications in Materials Science, Life Science, Earth Science, Food Science, and Engineering, Springer, 2017.
[18] P. Munier, K. Gordeyeva, L. Bergström, A.B. Fall, Directional Freezing of Nanocellulose Dispersions Aligns the Rod-Like Particles and Produces Low-Density and Robust Particle Networks, Biomacromolecules. 17 (2016) 1875–1881. https://doi.org/10.1021/acs.biomac.6b00304.
[19] J. Lee, Y. Deng, The morphology and mechanical properties of layer structured cellulose microfibril foams from ice-templating methods, Soft Matter 7 (2011) 6034–6040, https://doi.org/10.1039/C1SM05388D.
[20] I. Usov, G. Nyström, J. Adamcik, S. Handschin, C. Schütz, A. Fall, L. Bergström, R. Mezzenga, Understanding nanocellulose chirality and structure–properties relationship at the single fibril level, Nat. Commun. 6 (2015) 7564, https://doi.org/10.1038/ncomms8564.
[21] M.A. Hubbe, P. Tayeb, M. Joyce, P. Tyagi, M. Kehoe, K. Dimic-Misic, L. Pal, Rheology of Nanocellulose-rich Aqueous Suspensions: A Review, BioResources. 12 (2017) 9556-9661–9661. https://doi.org/10.15376/biores.12.4.9556-9661.
[22] E.J. Foster, R.J. Moon, U.P. Agarwal, M.J. Bortner, J. Bras, S. Camarero-Espinosa, K.J. Chan, M.J.D. Clift, E.D. Cranston, S.J. Eichhorn, D.M. Fox, W.Y. Hamad, L. Heux, B. Jean, M. Korey, W. Nieh, K.J. Ong, M.S. Reid, S. Renneckar, R. Roberts, J. A. Shatkin, J. Simonsen, K. Stinson-Bagby, N. Wanasekara, J. Youngblood, Current characterization methods for cellulose nanomaterials, Chem. Soc. Rev. 47 (8) (2018) 2609–2679, https://doi.org/10.1039/C6CS00895J.
[23] S. Toll, Note: On the tube model for fiber suspensions, J. Rheol. 37 (1993) 123–125, https://doi.org/10.1122/1.550460.
[24] S. Varanasi, R. He, W. Batchelor, Estimation of cellulose nanofibre aspect ratio from measurements of fibre suspension gel point, Cellulose 20 (4) (2013) 1885–1896, https://doi.org/10.1007/s10570-013-9972-9.
[25] V. Apostolopoulou-Kalkavoura, P. Munier, L. Dlugozima, V.-L. Heuthe, L. Bergström, Effect of density, phonon scattering and nanoporosity on the thermal conductivity of anisotropic cellulose nanocrystal foams, Sci. Rep. 11 (2021) 18685, https://doi.org/10.1038/s41598-021-98048-y.
[26] H. Sehaqui, M. Salajková, Q. Zhou, L.A. Berglund, Mechanical performance tailoring of tough ultra-high porosity foams prepared from cellulose I nanofiber suspensions, Soft Matter 6 (2010) 1824–1832, https://doi.org/10.1039/B927505C.
[27] E.R. Pounder, The Physics of Ice, Elsevier, 1965.
[28] P. Thévenaz, M. Unser, User-friendly semiautomated assembly of accurate image mosaics in microscopy, Microsc. Res. Tech. 70 (2) (2007) 135–146, https://doi.org/10.1002/jemt.20393.
[29] C.A. Schneider, W.S. Rasband, K.W. Eliceiri, NIH Image to ImageJ: 25 years of image analysis, Nat. Methods 9 (2012) 671–675, https://doi.org/10.1038/nmeth.2089.

[30] I. Arganda-Carreras, V. Kaynig, C. Rueden, K.W. Eliceiri, J. Schindelin, A. Cardona, H. Sebastian Seung, Trainable Weka Segmentation: a machine learning tool for microscopy pixel classification, Bioinformatics 33 (2017) 2424–2426, https://doi.org/10.1093/bioinformatics/btx180.
[31] M. Doube, M.M. Klosowski, I. Arganda-Carreras, F.P. Cordelières, R.P. Dougherty, J.S. Jackson, B. Schmid, J.R. Hutchinson, S.J. Shefelbine, BoneJ: free and extensible bone image analysis in ImageJ 47 (2010) 1076–1079.
[32] V. Boulos, V. Fristot, D. Houzet, L. Salvo, P. Lhuissier, Investigating performance variations of an optimized GPU-ported granulometry algorithm, in, in: Proceedings of the 2012 Conference on Design and Architectures for Signal and Image Processing, 2012, pp. 1–6.
[33] O. Bouaziz, J.P. Masse, S. Allain, L. Orgéas, P. Latil, Compression of crumpled aluminum thin foils and comparison with other cellular materials, Mater. Sci. Eng., A 570 (2013) 1–7, https://doi.org/10.1016/j.msea.2013.01.031.
[34] S. Deville, S. Deville, Freeze-casting of porous biomaterials: structure properties and opportunities, Materials 3 (2010) 1913–1927, https://doi.org/10.3390/ma3031913.
[35] R. Dash, Y. Li, A.J. Ragauskas, Cellulose nanowhisker foams by freeze casting, Carbohydr. Polym. 88 (2) (2012) 789–792, https://doi.org/10.1016/j.carbpol.2011.12.035.
[36] H. Bai, Y. Chen, B. Delattre, A.P. Tomsia, R.O. Ritchie, Bioinspired large-scale aligned porous materials assembled with dual temperature gradients, Sci. Adv. 1 (2015), https://doi.org/10.1126/sciadv.1500849 e1500849.
[37] L.J. Gibson, M.F. Ashby, Cellular Solids: Structure and Properties, Cambridge University Press, 1999.
[38] Z.M. Ali, L.J. Gibson, The structure and mechanics of nanofibrillar cellulose foams, Soft Matter 9 (5) (2013) 1580–1588, https://doi.org/10.1039/C2SM27197D.
[39] K.L. Scotti, D.C. Dunand, Freeze casting – A review of processing, microstructure and properties via the open data repository, FreezeCasting.net, Prog. Mater Sci. 94 (2018) 243–305, https://doi.org/10.1016/j.pmatsci.2018.01.001.
[40] M.F. Ashby, D. Cebon, Materials selection in mechanical design, Le, J. Phys. IV 03 (C7) (1993) C7-1–C7-9.
[41] X. Yang, E.D. Cranston, Chemically Cross-Linked Cellulose Nanocrystal Aerogels with Shape Recovery and Superabsorbent Properties, Chem. Mater. 26 (20) (2014) 6016–6025, https://doi.org/10.1021/cm502873c.
[42] K.J. De France, T. Hoare, E.D. Cranston, Review of Hydrogels and Aerogels Containing Nanocellulose, Chem. Mater. 29 (11) (2017) 4609–4631, https://doi.org/10.1021/acs.chemmater.7b00531.